



On Microstructure and Mechanical Properties of a Low-Carbon Low-Alloy Steel Block Fabricated by Wire Arc Additive Manufacturing

Mehran Rafieezad , Alireza Vahedi Nemani, Mahya Ghaffari, and Ali Nasiri

Submitted: 18 December 2020 / Revised: 1 February 2021 / Accepted: 6 February 2021 / Published online: 2 March 2021

In this study, wire arc additive manufacturing process is employed to fabricate a low-carbon low-alloy steel block, using an ER70S-6 solid wire. Three sets of samples with different orientations, including perpendicular (Vertical), parallel (Horizontal), and 45° (45-degree) relative to the deposition plane, were prepared in order to investigate the anisotropy in mechanical properties and microstructure of the fabricated part. Both Horizontal and 45-degree samples showed a uniform microstructure containing mostly ferritic grains with a small volume fraction of pearlite at their grain boundaries. Differently, a periodic microstructure was detected in the Vertical sample, consisting of a combination of acicular ferrite, bainite, and allotriomorphic ferrite formed in the interlayer regions in addition to polygonal ferrite within the melt pools' center. Moreover, the uniaxial tensile and Charpy impact results exhibited isotropic tensile, yield, elongation, and impact properties for both Horizontal and 45-degree samples; however, the Vertical sample showed a lower mechanical performance. The improved mechanical properties of the Horizontal and 45-degree samples were correlated to their uniform ferritic microstructure.

Keywords additive manufacturing (AM), low-carbon low-alloy steel, mechanical properties, microstructure, wire arc additive manufacturing (WAAM)

1. Introduction

Additive Manufacturing (AM) is a rapidly developing technology by which 3D components are produced through layer-by-layer deposition of the metallic, polymeric, or even ceramic materials using feedstock powder particles or solid wires (Ref 1). The metal AM process can be categorized based on the implemented heating source into two main categories, i.e., beam-based methods, such as selective laser melting (SLM) or electron beam melting (EBM), and arc-based technologies, such as wire arc additive manufacturing (WAAM) (Ref 2). Although the WAAM technology has not been completely industrialized yet, it has gained substantial attention in different industries, including aerospace, marine, and oil and

gas for the fabrication of meter-scale metallic components for structural applications (Ref 2, 3). As compared to other AM technologies, WAAM is mainly identified by its low capital cost, unlimited build envelope, and significantly high deposition rate (3–8 kg/h), leading to substantial reduction in the fabrication time (Ref 2). The common WAAM processes implement either a gas metal arc (GMA), gas tungsten arc (GTA), or plasma arc (PA) as the heat source (Ref 4–6). Cold metal transfer (CMT) is also a new variation of GMA technology and widely adopted as the heat source to produce WAAM components (Ref 7, 8).

Despite the cost-saving advantage of WAAM technology in fabrication of large-scale components from a wide range of materials, the high heat input and nonuniform solidification rate associated with the process lead to microstructural inhomogeneity and the anisotropy of the mechanical properties (Ref 4, 9, 10). Wu *et al.* (Ref 11) reported a highly anisotropic tensile strength for a thin wall 316 L stainless steel fabricated by GMA-WAAM. It has been reported that the high temperature gradient, fast cooling rate, and sequential heating and cooling cycles experienced by components during WAAM can impact the final microstructure, leading to a heterogeneous grain structure and anisotropic mechanical properties (Ref 12–14). Even reducing the heat input by implementing the CMT-WAAM technology for the fabrication of a Cr-Mn type steel was not found to be an effective approach to hinder the anisotropy in mechanical properties (Ref 15). It is well accepted that the WAAM processing parameters directly impact the in-situ thermal history during solidification of the part, determining the final microstructure and ultimately the part's mechanical performance (Ref 16, 17). As one of the less studied processing parameters, scanning or deposition pattern is an important factor that affects the thermal history, microstructural characteristics, and mechanical performance of AM components (Ref 18). In the WAAM technology, processing parameters, such as heat input (Ref 19), post-printing thermal treatment (Ref 20),

This invited article is part of a special topical focus in the *Journal of Materials Engineering and Performance* on Additive Manufacturing. The issue was organized by Dr. William Frazier, Pilgrim Consulting, LLC; Mr. Rick Russell, NASA; Dr. Yan Lu, NIST; Dr. Brandon D. Ribic, America Makes; and Caroline Vail, NSW Carderock.

Mehran Rafieezad, Faculty of Engineering and Applied Science, Memorial University of Newfoundland, St. John's, NL A1B 3X5, Canada; **Alireza Vahedi Nemani** and **Mahya Ghaffari**, Department of Mechanical Engineering, Dalhousie University, 1360 Barrington St, Halifax, NS B3H 4R2, Canada; and **Ali Nasiri**, Faculty of Engineering and Applied Science, Memorial University of Newfoundland, St. John's, NL A1B 3X5, Canada; and Department of Mechanical Engineering, Dalhousie University, 1360 Barrington St, Halifax, NS B3H 4R2, Canada. Contact e-mail: mrafieezad@mun.ca.

and size of the deposited wire (Ref 21) have been widely studied to tailor the microstructure and mechanical properties of the fabricated part. However, only limited research in the literature has attempted to investigate the deposition strategy's impact on the microstructural modification and mechanical properties, especially for low-carbon low-alloy steels with broad applications for the pipeline, casting, and forgings (Ref 22). Focusing on investigating the impact of deposition strategy on the microstructural modifications and the resultant mechanical properties, the present study has adopted a stripe scanning strategy with 90° rotation between consecutive layers to fabricate an ER70S-6 block using WAAM technology as compared to all-y scanning strategy commonly reported in the literature. The impact of the adopted deposition strategy on anisotropy in mechanical properties was investigated, utilizing tensile testing, impact testing, and fractography at different orientations of the fabricated block, i.e., vertical, horizontal, and 45° relative to the sample's building plane.

2. Experimental Procedure

2.1 Materials and Fabrication Procedures

A cuboid block of ER70S-6 alloy (Fig. 1b) was fabricated following a stripe strategy with a 90° rotation between successive layers using a FANUC ARC Mate® 50iD/7L 6-axis robotic arm equipped with a GMA torch and a Lincoln Electric Power Wave® R350 power source as shown in

Fig. 1(a). In order to minimize the surface irregularities and heat input during the process, an advanced surface tension transfer (STT) mode was employed. Each deposited layer in X-Y plane contains 40 individual beads with a length of 120 mm and a 3 mm center-to-center overlap, leading to the overall width of 120 mm. The total height of the part is 200 mm, comprising 40 consecutive layers with an average height of ~ 5 mm for each deposited layer. To control the impacts of complex thermal cycles associated with the WAAM process on the microstructure of the previously deposited layers, after each X-Y layer deposition, a 10-min interlayer dwell time was applied during the fabrication. Moreover, the presented schematic pattern in Fig. 1(c) shows the positions where Horizontal, Vertical, and 45-degree tensile and impact test samples were machined from the WAAM fabricated block. A 0.035 in. diameter ER70S-6 wire (0.06–0.15 wt.% C, 1.40–1.85 wt.% Mn, 0.80–1.15 wt.% Si, and Bal. Fe) was utilized as the feedstock material. The detailed process parameters can be found in the previous authors' publication (Ref 9).

2.2 Microstructural Characterization and Mechanical Properties

The microstructural characterization and investigation of possible formed microstructural inhomogeneity in the fabricated component were carried out on three samples prepared from different orientations of parallel, perpendicular, and 45° with respect to the deposition plane (X-Y), denoted by Horizontal, Vertical, and 45-degree samples, respectively. Standard grinding and polishing procedures for steels were

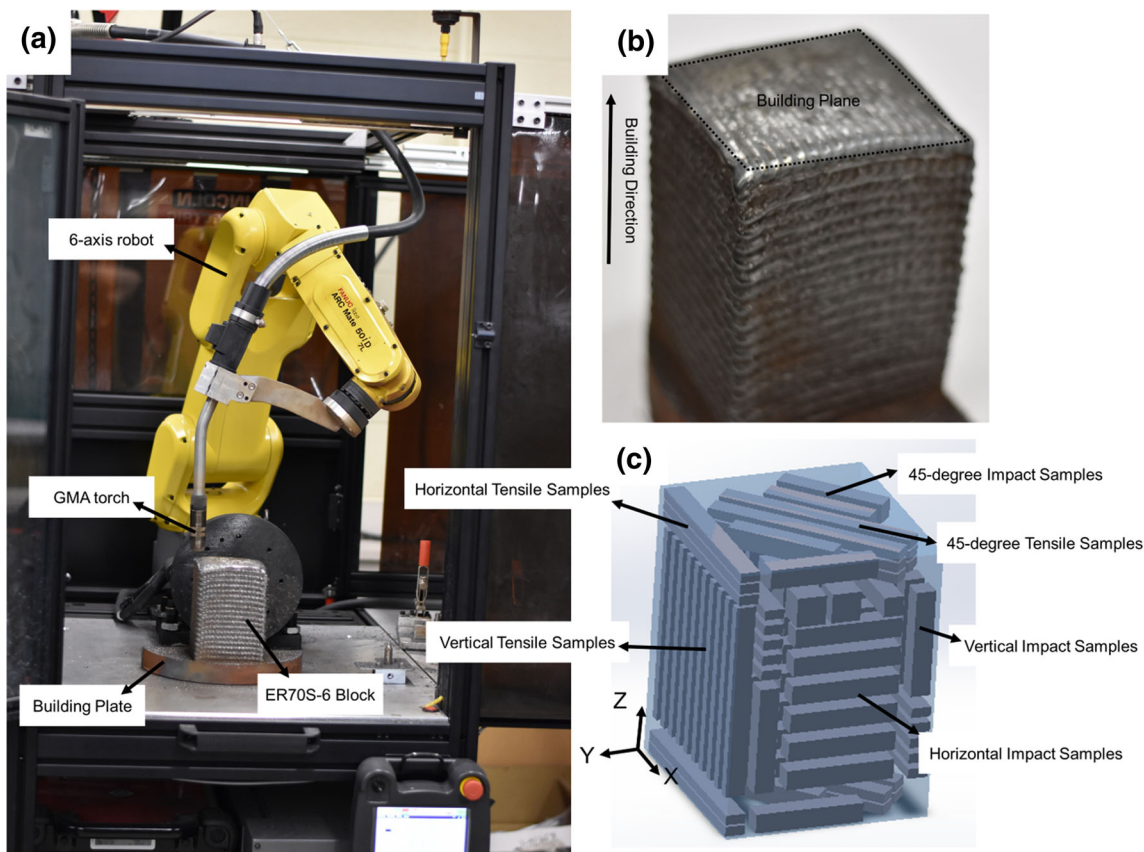


Fig. 1 (a) The robotic WAAM platform, (b) the fabricated block using WAAM method, (c) schematic drawing of the WAAM-ER70S-6 steel block showing the position of tensile and impact testing samples

implemented using a Tegramin-30 Struers auto-grinder/polisher. In order to reveal the microstructure, the polished samples were etched using 5% Nital as the etchant. The microstructure of all samples was investigated using an optical microscope (Nikon Eclipse 50i), and a field emission scanning electron microscope (SEM) (FEI MLA 650FEG). Electron backscatter diffraction (EBSD) analysis was also performed over a large area of $4000 \times 600 \mu\text{m}^2$ with a step size of $1.5 \mu\text{m}$ and a tilt angle of 70° , using a Nordlys II HKL EBSD detector, Oxford Instruments. The tensile test samples were made based on the ASTM E8m-04 standard sub-size specimen (Ref 23) and tested using a tensile strength testing instrument (Instron 5585H load frame) at the crosshead speed of 8 mm/min, and an extensometer to record strain data. The samples for the Charpy impact tests were made according to ASTM E23–18 (Ref 24). The absorbed energy by each sample during fracture was obtained at six different temperatures, i.e., -146 , -100 , -20 , 0 , 23 °C (room temperature), and 98 °C using an automatic impact testing apparatus (a JBS-300 machine) with the maximum capacity of 300 J. The fractured surfaces of both tensile and impact test samples from all three directions were also analyzed using the SEM.

3. Results and Discussion

3.1 Microstructural Characterization

Figure 2 shows the cross-sectional overview of the WAAM-ER70S-6 steel block taken from different orientations (from prepared gage length of the tensile samples prior to testing), revealing the microstructural variations resulted from the implemented 90° rotation deposition strategy. Optical micrographs in Horizontal and 45-degree directions (Fig. 2a and b) illustrate a uniform microstructure with almost no imperfection, such as pores and cracks, within the entire cross section,

indicating the formation of a sound and defect-free AM part on the X-Y plane with a clear metallurgical bonding between the neighboring tracks. The microstructures of the Horizontal and 45-degree samples were characterized with a relatively uniform microstructure without a significant grains morphology alteration between the tracks, attributed to the high interlayer temperature and consequently the lower interpass cooling rates, resulted from the center-to-center overlap of the tracks in the deposition (X-Y) plane. However, the Vertical sample (Fig. 2c) shows a periodic nonuniform microstructure containing a variety of interlayer discontinuities, such as lack of fusion and porosities, formed particularly along the inter-layers' regions perpendicular to the building direction. A banded structure comprised of polygonal ferrite and a mixture of acicular ferrite (AF), bainite (B), and allotriomorphic ferrite (α) (as shown in Fig. 3) was found to form between consecutive layers, resulting from the nonuniform cooling rate of each melt pool in the areas near to its boundaries as compared to the center. Moreover, the Vertical sample has experienced a 10 min dwelling time between deposition of successive layers along the Z-direction, resulted in the nonhomogeneous energy input and consequently the formation of the periodic microstructure as shown in Fig. 2(c). Similar observations were reported in a previous study by Ge *et al.* (Ref 25) for a WAAM-2Cr13 thin wall fabricated with a long dwelling time (210 s), which was characterized by a periodic microstructure composed of martensite laths in a ferritic matrix. Differently, adopting a short dwelling time (30 s) during fabrication was reported to create a uniform ferritic microstructure (Ref 25). It is notable that the height of the banded microstructures is similar to the height of each deposited layer (~ 3 mm).

Figure 3(a) schematically represents two consecutive deposited beads along the Z-direction, showing three distinguishable regions with distinct microstructures, i.e., melt pool center, melt pool boundary, and a heat affected zone (HAZ) in the previously deposited layer (Bead 1). Figure 3(b) shows the

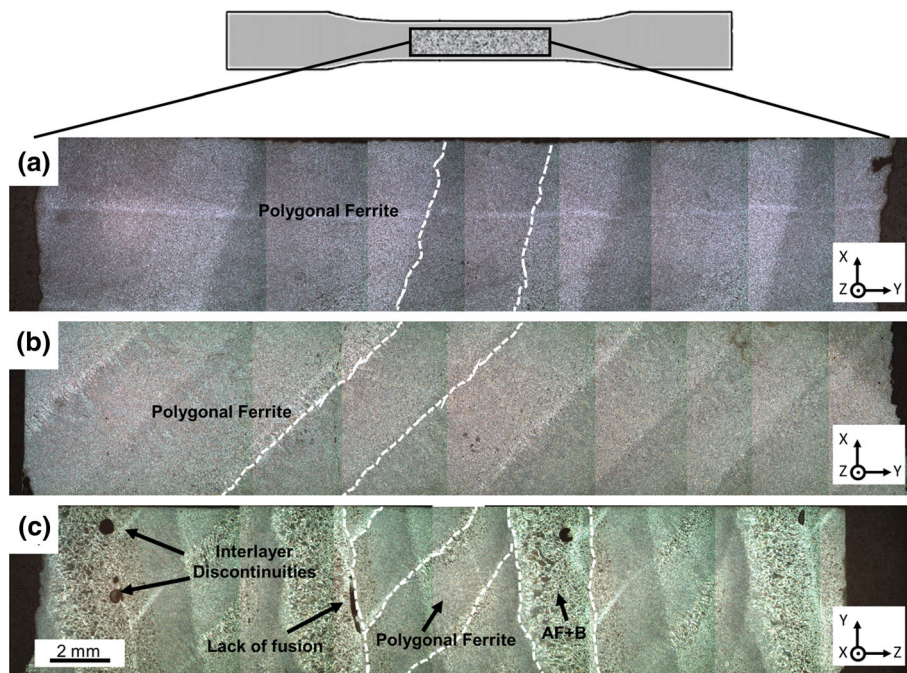


Fig. 2 Optical micrographs taken from the overall cross-sectional overview of the (a) horizontal, (b) 45-degree, and (c) vertical samples

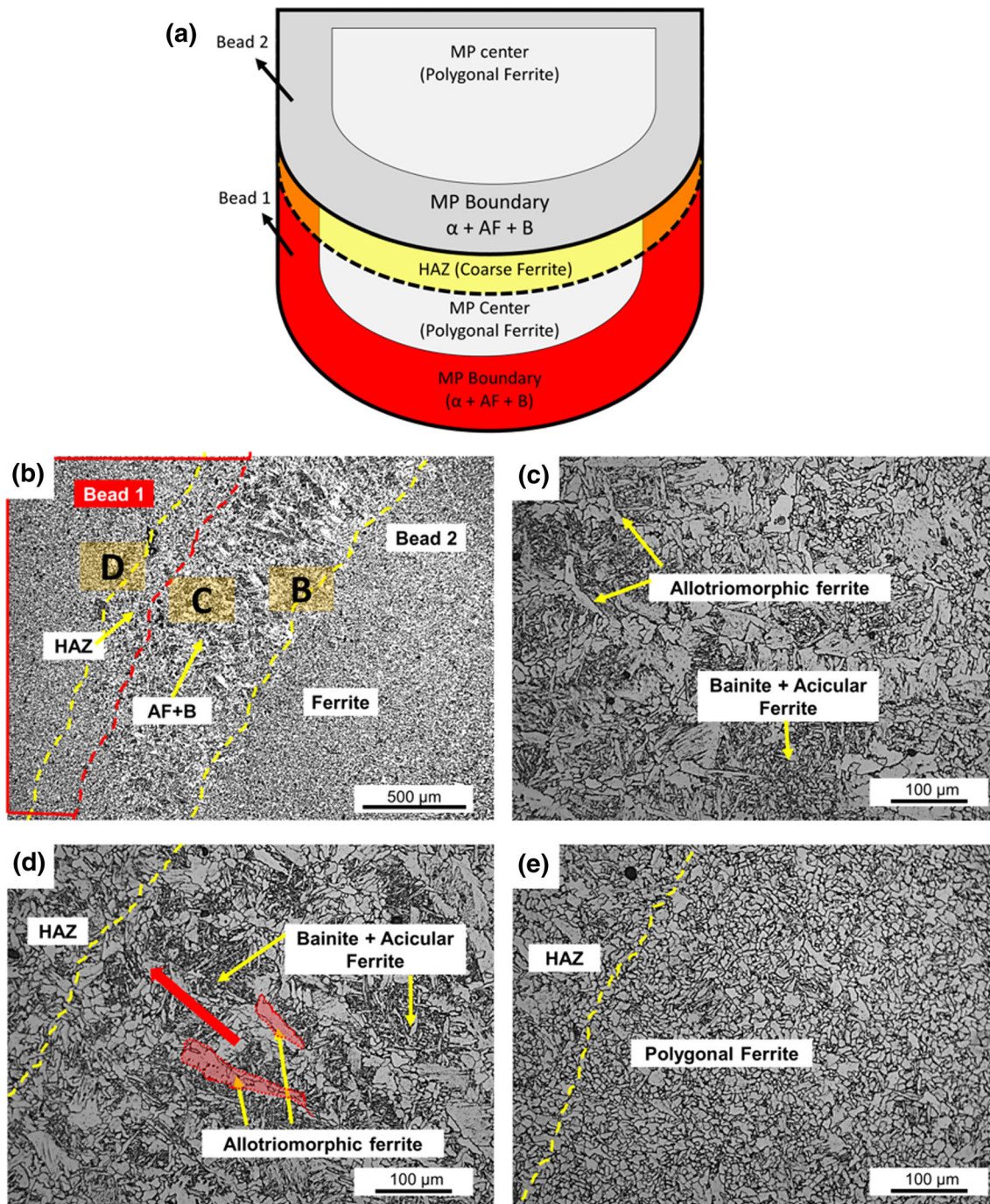


Fig. 3 (a) Schematic representation of two consecutive deposited beads, Optical micrographs taken from (b) the fusion line and center of the melt pool, and higher magnification of the (c) melt pool boundary shown as C in (b), (d) fusion line shown as D in (b), and (e) melt pool center shown as E in (b)

overall microstructure of the Vertical sample in the vicinity of a melt pool boundary, in which two successive beads and their corresponding HAZ are noticeable, revealing the variation of microstructure from an area adjacent to a fusion line (Fig. 3d) toward the middle of the melt pool (Fig. 3e). The microstructural transition from a uniform and fine polygonal ferritic (F) structure at the center of the melt pool to a combination of acicular ferrite (AF), bainite (B), and allotriomorphic ferrite (shaded areas in Fig. 3d) microstructure in the melt pool boundary (Fig. 3c and d) is evident. Moving closer to the fusion

line in the melt pool boundary areas revealed columnar grains of acicular ferrite, bainite, and allotriomorphic ferrite, elongated along the heat dissipation direction (the red arrow in Fig. 3d) during solidification. However, the dominant microstructure of each melt pool is fine polygonal ferrite with a slight volume fraction of pearlite on the grain boundaries (Fig. 3e).

In complementary to the performed optical microscopy investigation, SEM and EBSD analyses were also carried out (Fig. 4) for detailed microstructural characterization of the samples. The EBSD inverse pole figure (IPF) map from the

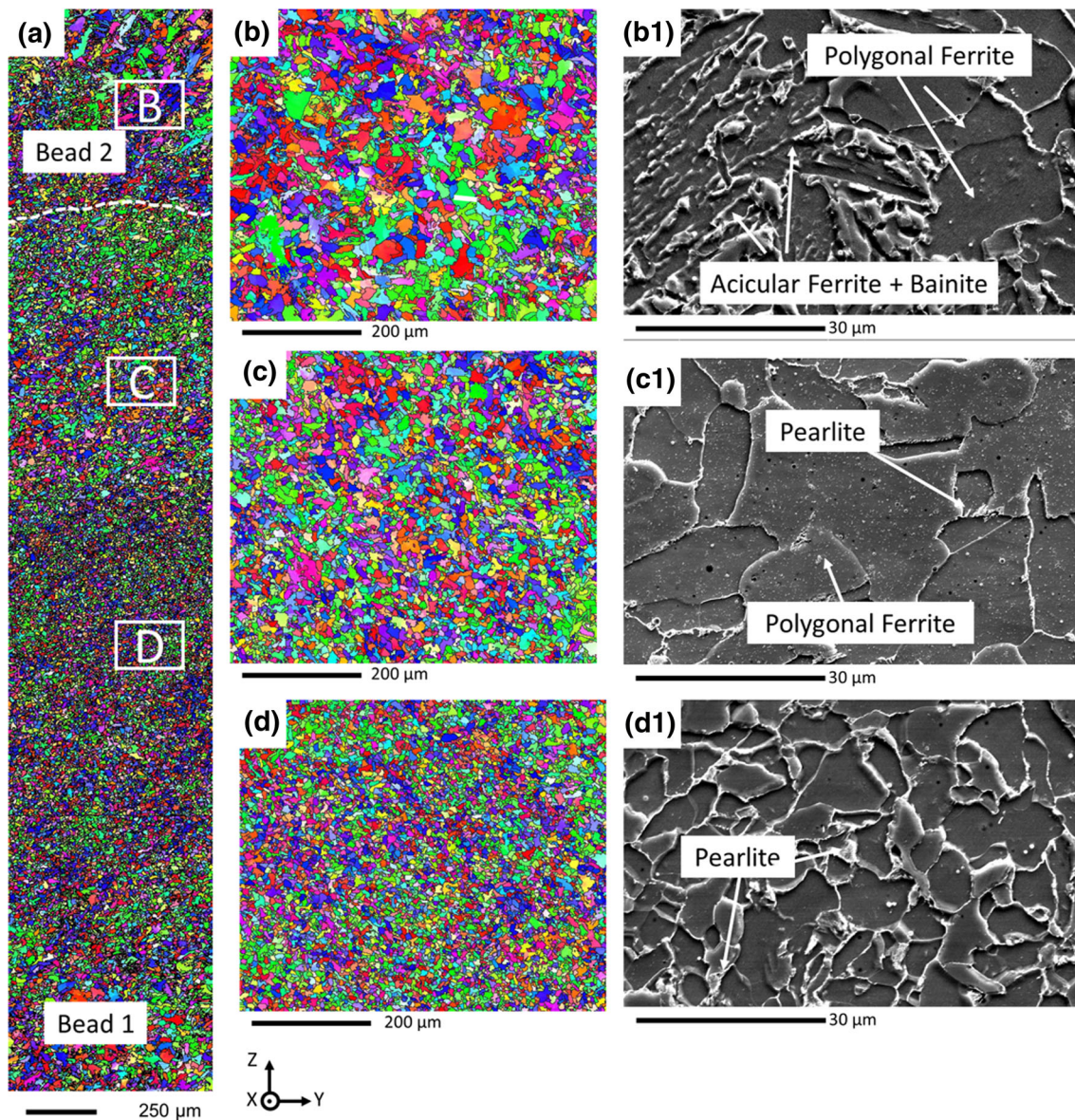


Fig. 4 The EBSD inverse pole figure maps taken from (a) the entire cross-sectional overview along building direction of the WAAM-ER70SR-6 sample, (b) the higher magnification of the enclosed area in (a) noted by B, (b1) the SEM image from the same area of the (b), (c) the higher magnification of the enclosed area in (a) noted by C, (c1) the SEM image from the same area of the (c), (d) the higher magnification of the enclosed area in (a) noted by D, (d1) the SEM image from the same area of the (d)

entire microstructure between two adjacent layers along the building direction (Z-axis) (Fig. 4a) shows the overall grains' orientation/misorientation, size, and aspect ratio. The variation of the grain size and morphology can be clearly seen along the entire cross section in the Vertical sample. In Fig. 4(a), there are regions (region B) with coarser grain structure with the average grain size of $38.88 \pm 1.54 \mu\text{m}$ located at the melt pool boundaries (Fig. 4b). The SEM micrographs from the same area (Fig. 4b1) revealed the formation of the nonequilibrium AF + B constituents adjacent to the melt pool boundary, resulted from the faster cooling rate of the fusion zone at the melt pool boundaries as compared to the center of the melt pool. Differently, the melt pool's center was characterized by equiaxed (aspect ratio < 3) and randomly oriented ferritic grain structure with the average grain size of $7.23 \pm 0.34 \mu\text{m}$ (Fig. 4d). The SEM micrograph from the melt pool center

(Fig. 4d1) confirmed the formation of the PF grains with a very small volume fraction of lamellar pearlite (P) ($11.44 \pm 0.47\%$) formed at the grain boundaries, which is the predominant microstructure over the entire fabricated block. The grain structure in HAZ (Figs. 4c and 4c1) consists of coarser ferrite grains ($10.86 \pm 0.25 \mu\text{m}$) as compared to the center of the melt pool, which is a direct consequence of the grain boundaries migration in the previously deposited bead, triggered by the significantly high temperature from deposition of a new layer (Ref 4).

3.2 Mechanical Properties

The orientation of tensile and impact testing samples in the horizontal, vertical, and 45° directions in the fabricated block is presented in Fig. 1(c). Figure 5(a) shows the engineering tensile stress-strain graphs for the Vertical, Horizontal, and 45° -degree

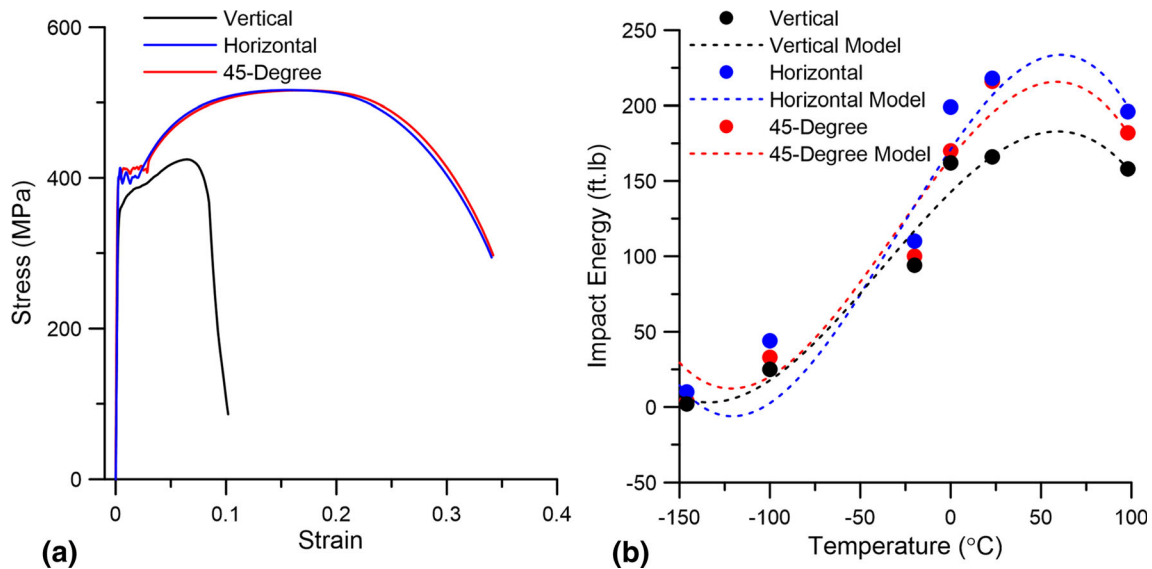


Fig. 5 (a) the stress-strain curves and (b) the absorbed impact energy for the horizontal, vertical, and 45-degree samples

samples. At each orientation, at least five samples were tested to ensure reproducibility of the results.

The majority of the tensile graphs displayed the common yield point phenomenon frequently seen in low-carbon and mild steels (Ref 26, 27). A similar discontinuous yielding characteristic has been reported for other WAAM fabricated ER70S-6 parts as well (Ref 4, 9, 27). Along the deposition plane, the Horizontal and 45-degree samples showed a uniform deformation with a similar ductile failure during tensile testing. Moreover, as shown in Fig. 2(a) and (b), since the Horizontal and 45-degree samples have a uniform microstructure, variation of MP boundaries orientation with respect to the tensile direction (90° and 45° for Horizontal and 45-degree sample, respectively) has not affected the ultimate tensile strength (UTS), yield strength (YS), and elongation of the samples. As a result, similar average UTS, YS, and elongation values (406 ± 23 MPa, 524 ± 13 MPa, and $37 \pm 3\%$, respectively) were obtained for both samples, confirming the isotropic mechanical performance of the fabricated block on its X-Y plane. On the other hand, the average UTS, YS, and elongation values of the Vertical samples were found to be lower than those of the other two samples (386 ± 26 MPa, 405 ± 22 MPa, and $10 \pm 2\%$, respectively), confirming the anisotropic tensile properties of the WAAM manufactured block. The lower tensile strength and elongation properties of the Vertical sample can be correlated to either microstructural variations across the building direction or pre-existing interlayer imperfections, which are, in turn, associated with the heat dissipation characteristics and the implemented interlayer dwelling time during manufacturing of the part, consistent with the previous studies (Ref 4, 9, 12, 25).

The Charpy V-notch impact results for the Horizontal, 45-degree, and Vertical samples performed at six different temperatures of -146 , -100 , -20 , 0 , 23 °C (room temperature), and 98 °C are given in Fig. 5(b). The fitted curves to the obtained experimental data points represent cubic functions with the error parameter value (R^2) above 0.90, featuring a Ductile to Brittle Transition Temperature (DBTT) for the fabricated alloy at ~ -20 °C. The results also confirm that the DBTT is constant and independent from the samples' orientations. The average values of the absorb energy for the

Horizontal and 45-degree samples at all seven temperatures are higher than those of the Vertical sample, ascribed to their uniform ferritic and defect-free structure. The formation of uniform and smaller ferritic grains in Horizontal and 45-degree samples promotes both yield strength and tensile strength and further improves ductile fracture mechanisms, while the Vertical sample with periodic microstructure of acicular ferrite and bainitic are expected to have a more brittle nature and be more susceptible to crack propagation (Ref 28, 29).

To further investigate the fracture performance of the fabricated samples, the fracture surfaces of all samples after uniaxial tensile and impact testing were analyzed and shown in Fig. 6. The SEM fractographs of the Horizontal and 45-degree samples (Fig. 6a and b) mainly showed the characteristics of dimple-like fracture, confirming an extended plastic deformation and ductile fracture. Differently, the Vertical sample (Fig. 6c) showed inclusions combined with smaller and shallower dimples, indicating that it experienced a lower degree of plastic strain before failure. Using Energy-Dispersive-x-ray Spectroscopy (EDS), the inclusions were characterized to be mainly composed of MnO-SiO_2 , commonly reported to form in ferrous alloys weld metals (Ref 30). These inclusions in the Vertical sample can be formed due to the slag entrapment between successive layers. A comparison between the fracture surfaces after the impact test at room temperature revealed some nearly flat surfaces in the Vertical samples (Fig. 6f), representing relatively fast crack propagation and occurrence of a rapid cleavage fracture (Ref 31). However, the Horizontal and 45-degree samples (Fig. 6d and e) showed no cleavage on their fractured surfaces. Another noticeable high absorbed energy feature on the fracture surfaces of the Horizontal and 45-degree samples is the secondary cracks, resulted from energy dissipation in the material during the dislocations movements (Ref 32).

3.3 Comparisons with the WAAM-ER70S-6 thin-wall Fabricated Using All-y Scanning Strategy

To better understand the impact of deposition strategy and sample size on the microstructure and mechanical properties of the fabricated block, comparisons were made between the microstructure and mechanical properties of the block fabri-

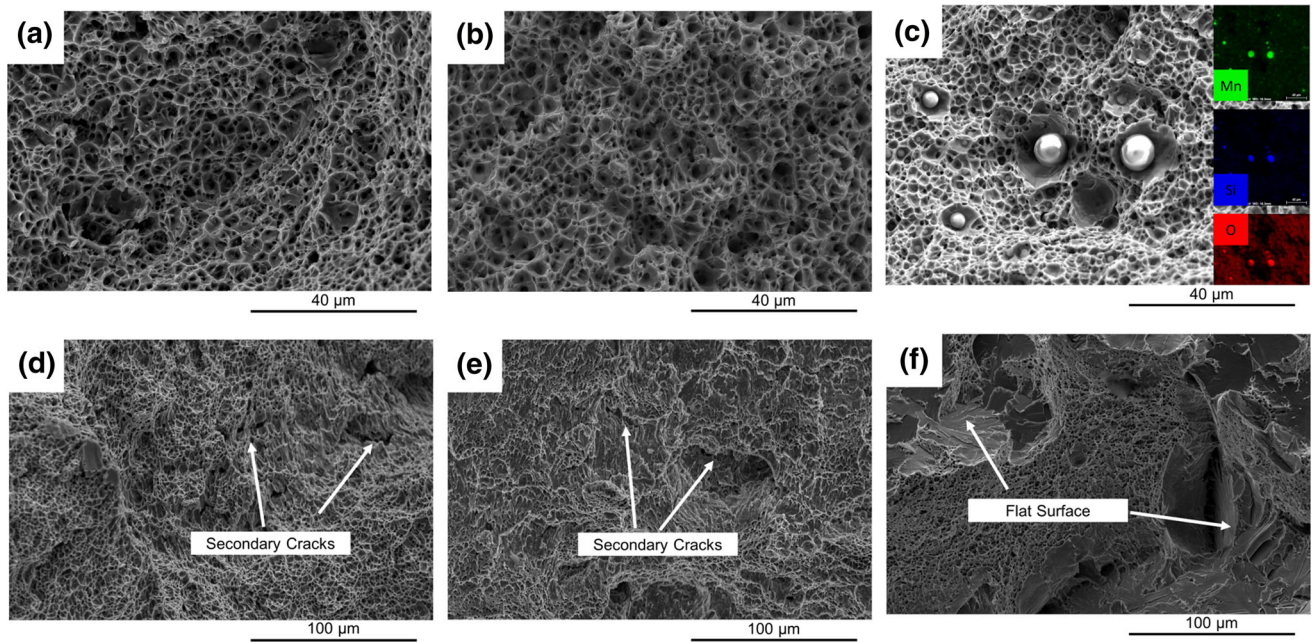


Fig. 6 SEM micrographs taken from the fractured surfaces after uniaxial tensile testing of (a) horizontal, (b) 45-degree, and (c) vertical samples and after impact testing of (d) horizontal, (e) 45-degree, and (f) vertical samples at room temperature (23 °C)

cated with a 90° deposition strategy studied herein and a thin-wall fabricated by all-y scanning strategy studied in the authors' previous works (Ref 4, 9).

The formation of the AF+B microstructure near the melt pool boundaries and fine polygonal ferrite with small amount of pearlite in its grain boundaries as a primary microstructure of the melt pool center have been also observed in a WAAM-ER70S thin-wall fabricated using all-y scanning strategy (Ref 4, 9). However, using a 90° deposition strategy led to the formation of the periodic microstructure along the building direction, which was not detected in the thin-wall fabricated sample (Ref 4, 9). Moreover, the grain size variations for the extreme fine and coarse regions of the thin-wall sample were reported to be in the range of $\sim 4.94 \mu\text{m}$ to $\sim 15.76 \mu\text{m}$, respectively. The thin-wall sample with 22 mm width has experienced significantly lower heat accumulation and a faster cooling rate as compared to the block sample with 120 mm width. Therefore, in the thin-wall sample, all the deposited layers have faced almost the same thermal cycles, giving rise to a finer and more uniform microstructure than the block sample.

Furthermore, the anisotropy in mechanical properties of the Horizontal and Vertical samples detected for the block sample was also detected in the thin-wall sample. The reported average values of UTS, YS, and elongation for Horizontal and Vertical samples were $396 \pm 26 \text{ MPa}$, $503 \pm 21 \text{ MPa}$, $35 \pm 2\%$, $402 \pm 23 \text{ MPa}$, $502 \pm 19 \text{ MPa}$, $12 \pm 3\%$, respectively (Ref 4, 9). The measured lower UTS and YS values for the Vertical sample in the block part than those in the thin-wall sample can be attributed to the formation of the periodic microstructure with sharp boundaries between the deposited layer and also the formation of substantial interpass defects in the vertical direction of the block sample. Moreover, the formation of the martensite-austenite (MA) constituent within the bainite lamellar structures was reported as a contributing factor to the improved tensile strength and degradation of the toughness in the thin-wall sample (Ref 4, 9). However, in this study, larger

geometrical features of the fabricated block create higher heat accumulation, leading to its slower cooling rate during solidification, which would consequently impact the final microstructure, level of interpass discontinuities, and suppress the MA micro-constituent formation (Ref 33).

4. Conclusions

In this study, the microstructure and mechanical characteristics of a block of ER70S-6 low-carbon low-alloy steel fabricated utilizing the WAAM technique with deposition strategy of 90° rotation between successive layers were measured and compared with the thin-wall sample of the same alloy fabricated using all-y scanning strategy. The following conclusions can be drawn:

1. The microstructure of the Horizontal and 45-degree samples contained mainly ferrite grains with a small volume fraction of pearlite formed at the grain boundaries.
2. A more heterogeneous microstructure was detected in the Vertical sample, composed of three distinct regions of fine polygonal ferritic grains formed in melt pools' centers, a combination of allotriomorphic ferrite and acicular ferrite and bainite in the melt pools' boundaries, and coarse polygonal ferritic grains in HAZ.
3. The EBSD results revealed that the overall microstructure was predominantly composed of randomly oriented equiaxed grains across the entire building direction. The slower cooling rate during solidification in the block sample resulted in coarsening of the average grain size by 60% as compared to the thin-wall sample.
4. The tensile test results of the Horizontal and 45-degree samples showed the isotropic YS, UTS, and elongation properties along the building plane of the fabricated WAAM-ER70S-6 block. However, the mechanical perfor-

mance was dropped in the Vertical sample, associated with the existence of the discontinuities in the interpass regions and heterogeneity of the microstructure along the vertical direction.

5. The average impact resistance of the Horizontal and 45-degree samples at different temperatures were similar and higher than that of the Vertical samples, dictated by the microstructural variations between the samples.
6. The fracture surfaces of Horizontal and 45-degree samples at room temperature revealed dimpled rupture characteristics and secondary cracks, suggesting a pure ductile fracture. However, the fracture surface of the Vertical sample showed smaller and shallower dimples, inclusions and some flat regions, confirming the reduced toughness of the fabricated sample along the building direction as compared to the building plane.

Acknowledgments

The authors acknowledge the support of Natural Sciences and Engineering Research Council of Canada (NSERC), Canada Research Chair (CRC) program, Memorial University of Newfoundland, and Dalhousie University for sponsoring this work.

References

1. W.E. Frazier, Metal Additive Manufacturing: A Review, *J. Mater. Eng. Perform.*, 2014, **23**(6), p 1917–1928
2. A. Taşdemir and S. Nohut, An Overview of Wire Arc Additive Manufacturing (WAAM) in Shipbuilding Industry, *Ships Offshore Struct.*, 2020 <https://doi.org/10.1080/17445302.2020.1786232>
3. A.V. Filippov, E.S. Khoroshko, N.N. Shamarin, N.L. Savchenko, E.N. Moskvichev, V.R. Utyaganova, E.A. Kolubaev, A.Y. Smolin and S.Y. Tarasov, Characterization of Gradient CuAl-B4C Composites Additively Manufactured Using a Combination of Wire-Feed and Powder-Bed Electron Beam Deposition Methods, *J. Alloys Compd.*, 2021, **859**, p 157824. <https://doi.org/10.1016/j.jallcom.2020.157824>
4. M. Ghaffari, A.V. Nemani, M. Rafieazad and A. Nasiri, Effect of Solidification Defects and HAZ Softening on the Anisotropic Mechanical Properties of a Wire Arc Additive-Manufactured Low-Carbon Low-Alloy Steel Part, *JOM*, 2019, **71**(11), p 4215–4224. <https://doi.org/10.1007/s11837-019-03773-5>
5. J.P. Oliveira, B. Crispim, Z. Zeng, T. Otori, F.M.B. Fernandes and R.M. Miranda, Microstructure and Mechanical Properties of Gas Tungsten Arc Welded Cu-Al-Mn Shape Memory Alloy Rods, *J. Mater. Process. Technol.*, 2019, **271**, p 93–100. <https://doi.org/10.1016/j.jmatprotec.2019.03.020>
6. F. Martina, J. Mehnen, S.W. Williams, P. Colegrove and F. Wang, Investigation of the Benefits of Plasma Deposition for the Additive Layer Manufacture of Ti-6Al-4V, *J. Mater. Process. Technol.*, 2012, **212**(6), p 1377–1386. <https://doi.org/10.1016/j.jmatprotec.2012.02.002>
7. Y. Wang, X. Chen, S. Konovalov, C. Su, A.N. Siddiquee and N. Gangil, In-Situ Wire-Feed Additive Manufacturing of Cu-Al Alloy by Addition of Silicon, *Appl. Surf. Sci.*, 2019, **487**, p 1366–1375. <https://doi.org/10.1016/j.apsusc.2019.05.068>
8. P.P. Nikam, D. Arun, K.D. Ramkumar and N. Sivashanmugam, Microstructure Characterization and Tensile Properties of CMT-Based Wire plus Arc Additive Manufactured ER2594, *Mater. Charact.*, 2020, **169**, p 110671. <https://doi.org/10.1016/j.matchar.2020.110671>
9. M. Rafieazad, M. Ghaffari, A.V. Nemani and A. Nasiri, Microstructural Evolution and Mechanical Properties of a Low-Carbon Low-Alloy Steel Produced by Wire Arc Additive Manufacturing, *Int. J. Adv. Manuf. Technol.*, 2019 <https://doi.org/10.1007/s00170-019-04393-8>
10. S. Li, J. Ning, G.-F. Zhang, L.-J. Zhang, J. Wu and L.-X. Zhang, Microstructural and Mechanical Properties of Wire-Arc Additively Manufactured Al-Zn-Mg Aluminum Alloy: The Comparison of as-

Deposited and Heat-Treated Samples, *Vacuum*, 2021, **184**, p 109860. <https://doi.org/10.1016/j.vacuum.2020.109860>

11. W. Wu, J. Xue, L. Wang, Z. Zhang, Y. Hu and C. Dong, Forming Process, Microstructure, and Mechanical Properties of Thin-Walled 316L Stainless Steel Using Speed-Cold-Welding Additive Manufacturing, *Metals (Basel)*, 2019 <https://doi.org/10.3390/met9010109>
12. A.V. Nemani, M. Ghaffari and A. Nasiri, Comparison of Microstructural Characteristics and Mechanical Properties of Shipbuilding Steel Plates Fabricated by Conventional Rolling versus Wire Arc Additive Manufacturing, *Addit. Manuf.*, 2020, **32**, p 101086. <https://doi.org/10.1016/j.addma.2020.101086>
13. M. Ghaffari, A.V. Nemani and A. Nasiri, Interfacial Bonding Between a Wire Arc Additive Manufactured 420 Martensitic Stainless Steel Part and Its Wrought Base Plate, *Mater. Chem. Phys.*, 2020, **251**, p 123199. <https://doi.org/10.1016/j.matchemphys.2020.123199>
14. A.V. Nemani, M. Ghaffari and A. Nasiri, On the Post-Printing Heat Treatment of a Wire Arc Additively Manufactured ER70S Part, *Materials (Basel)*, 2020 <https://doi.org/10.3390/ma13122795>
15. X. Zhang, Q. Zhou, K. Wang, Y. Peng, J. Ding, J. Kong and S. Williams, Study on Microstructure and Tensile Properties of High Nitrogen Cr-Mn Steel Processed by CMT Wire and Arc Additive Manufacturing, *Mater. Des.*, 2019, **166**, p 107611. <https://doi.org/10.1016/j.matdes.2019.107611>
16. J.P. Oliveira, A.D. LaLonde and J. Ma, Processing Parameters in Laser Powder Bed Fusion Metal Additive Manufacturing, *Mater. Des.*, 2020, **193**, p 108762. <https://doi.org/10.1016/j.matdes.2020.108762>
17. J.P. Oliveira, T.G. Santos and R.M. Miranda, Revisiting Fundamental Welding Concepts to Improve Additive Manufacturing: From Theory to Practice, *Prog. Mater. Sci.*, 2020, **107**, p 100590. <https://doi.org/10.1016/j.pmatsci.2019.100590>
18. L.N. Carter, C. Martin, P.J. Withers and M.M. Attallah, The Influence of the Laser Scan Strategy on Grain Structure and Cracking Behaviour in SLM Powder-Bed Fabricated Nickel Superalloy, *J. Alloys Compd.*, 2014, **615**, p 338–347. <https://doi.org/10.1016/j.jallcom.2014.06.172>
19. D. Wen, P. Long, J. Li, L. Huang and Z. Zheng, Effects of Linear Heat Input on Microstructure and Corrosion Behavior of an Austenitic Stainless Steel Processed by Wire Arc Additive Manufacturing, *Vacuum*, 2020, **173**, p 109131. <https://doi.org/10.1016/j.vacuum.2019.109131>
20. X. Fang, H. Li, X. Li, K. Huang, L. Zhang and B. Lu, Effect of Post Heat Treatment on the Microstructure and Mechanical Properties of Wire-Arc Additively Manufactured A357 Alloy Components, *Mater. Lett.*, 2020, **269**, p 127674. <https://doi.org/10.1016/j.matlet.2020.127674>
21. C. Wang, W. Suder, J. Ding and S. Williams, The Effect of Wire Size on High Deposition Rate Wire and Plasma Arc Additive Manufacture of Ti-6Al-4V, *J. Mater. Process. Technol.*, 2021, **288**, p 116842. <https://doi.org/10.1016/j.jmatprotec.2020.116842>
22. G.H. Majzoobi, A.H. Mahmoudi and S. Moradi, Ductile to Brittle Failure Transition of HSLA-100 Steel at High Strain Rates and Subzero Temperatures, *Eng. Fract. Mech.*, 2016, **158**, p 179–193. <https://doi.org/10.1016/j.engfracmech.2016.03.001>
23. ASTM E8M-04, Standard Test Methods for Tension Testing of Metallic Materials [Metric], (West Conshohocken, PA), ASTM International, 2008, doi:<https://doi.org/10.1520/E0008M-04>
24. A. E23-18, Standard Test Methods for Notched Bar Impact Testing of Metallic Materials, *ASTM Int.*, 2018, www.astm.org
25. J. Ge, J. Lin, H. Fu, Y. Lei and R. Xiao, Tailoring Microstructural Features of Wire Arc Additive Manufacturing 2Cr13 Part via Varying Inter-Layer Dwelling Time, *Mater. Lett.*, 2018, **232**, p 11–13. <https://doi.org/10.1016/j.matlet.2018.08.037>
26. N. Sridharan, M.W. Noakes, A. Nycz, L.J. Love, R.R. Dehoff and S.S. Babu, On the Toughness Scatter in Low Alloy C-Mn Steel Samples Fabricated Using Wire Arc Additive Manufacturing, *Mater. Sci. Eng. A*, 2018, **713**, p 18–27. <https://doi.org/10.1016/j.msea.2017.11.101>
27. B. Shassere, A. Nycz, M.W. Noakes, C. Masuo and N. Sridharan, Correlation of Microstructure and Mechanical Properties of Metal Big Area Additive Manufacturing, *Appl. Sci.*, 2019 <https://doi.org/10.3390/app9040787>
28. A. Waqas, X. Qin, J. Xiong, C. Zheng and H. Wang, Analysis of Ductile Fracture Obtained by Charpy Impact Test of a Steel Structure Created by Robot-Assisted GMAW-Based Additive Manufacturing, *Metals (Basel)*, 2019 <https://doi.org/10.3390/met9111208>

29. Y. Zhao, X. Tong, X.H. Wei, S.S. Xu, S. Lan, X.-L. Wang and Z.W. Zhang, Effects of Microstructure on Crack Resistance and Low-Temperature Toughness of Ultra-Low Carbon High Strength Steel, *Int. J. Plast.*, 2019, **116**, p 203–215. <https://doi.org/10.1016/j.ijplas.2019.01.004>
30. G. Chen, H. Luo, H. Yang, Z. Han, Z. Lin, Z. Zhang and Y. Su, Effects of the Welding Inclusion and Notch on the Fracture Behaviors of Low-Alloy Steel, *J. Mater. Res. Technol.*, 2019, **8**(1), p 447–456. <https://doi.org/10.1016/j.jmrt.2018.04.005>
31. X. Xu, S. Ganguly, J. Ding, S. Guo, S. Williams and F. Martina, Microstructural Evolution and Mechanical Properties of Maraging Steel Produced by Wire+arc Additive Manufacture Process, *Mater. Charact.*, 2017, **5**, p 10
32. A. Pineau, A.A. Benzerga and T. Pardoen, Failure of Metals I: Brittle and Ductile Fracture, *Acta Mater.*, 2016, **107**, p 424–483. <https://doi.org/10.1016/j.actamat.2015.12.034>
33. N. Huda, A.R.H. Midawi, J. Gianetto, R. Lazor and A.P. Gerlich, Influence of Martensite-Austenite (MA) on Impact Toughness of X80 Line Pipe Steels, *Mater. Sci. Eng. A*, 2016, **662**, p 481–491. <https://doi.org/10.1016/j.msea.2016.03.095>

Publisher's Note Springer Nature remains neutral with regard to jurisdictional claims in published maps and institutional affiliations.